Ethiopian Journal of Water Science and Technology (EJWST)

DOI: https://doi.org/10.59122/EJWST850

Vol. 9, 2026, Pages: 123~150 ISSN (Print): 2220-7643

Spatiotemporal Variability and Trends of Precipitation and Temperature in Relation to Sea Surface Temperature Teleconnections over Central Ethiopia's Regional State

Gezahegn Bekele Tashebo[1,3 *] | Tadesse Terefe Zeleke[2] | Bisrat Elias Cholo[1]

[1]Arba Minch University, Water Technology Institute, Faculty of Meteorology & Hydrology, Arba Minch, P.O. Box 21, Ethiopia

[2]International Center for Tropical Agriculture (CIAT), Addis Ababa P.O. Box 5689, Ethiopia

[3]Ethiopian Meteorological Institute, Addis Ababa, P.O. Box, 1090, Ethiopia

[*]Correspondence: Gezahegn Bekele (terrykonjo669@gmail.com)

ABSTRACT

Climate variability and climate change significantly affect poor countries whose economies depend on climate-sensitive sectors with limited adaptive capacity. This study examined the spatiotemporal variability and trends of precipitation and temperature in relation to sea surface temperature (SST) teleconnections over Central Ethiopia Regional State (CERS). Monthly precipitation data from Climate Hazards Group CHIRPS, temperature data from Climatic Research Unit CRU-TS4.08, and global SST data for 1981–2023 were analyzed using the Standardized Anomaly Index (SAI), Mann–Kendall trend test, Empirical Orthogonal Function (EOF), and Pearson correlation analysis. Results showed that Kiremt (JJAS) contributes 57.7% of annual rainfall, while Belg (FMAM) and Bega (ONDJ) contribute 32% and 10.3%, respectively. No statistically significant seasonal precipitation trends were detected at $p = 0.05$ although September and November rainfall exhibited significant increasing trends. EOF analysis revealed that the first three modes explained 84.23% and 92.16% of total rainfall variance during JJAS and FMAM, respectively. JJAS rainfall showed strong relationships with Pacific and Indian Ocean SSTs, whereas FMAM variability was strongly influenced by large-scale SST patterns. Temperature analysis indicated significant warming trends in minimum, mean, and maximum temperatures across all seasons. Annual temperature anomalies shifted from relatively cooler conditions in the early 1980s to persistent warming in recent decades. The study recommends season-specific agricultural planning, climate-resilient water management, improved climate information and early warning systems, and location-specific adaptation strategies.

Keywords: CERS; precipitation variability; temperature trends; sea surface temperature (SST); teleconnection; Empirical Orthogonal Function (EOF); Mann–Kendall trend test.

Received: 11 January, 2026; Accepted: 01 May, 2026 Published: 11, June 2026

1 INTRODUCTION

Climate variability and change significantly affect many poor countries that depend on climate sensitive sectors with limited ability to adapt (Mesfin et al., 2020; Worku et al., 2022). The average temperature of the Earth has increased by 0.8 °C in the last century, with the last 35 years seeing the greatest of this increase (Dawson & Spannagle, 2008). The past trends of climate fluctuation and change in Ethiopia were studied by several researchers. For example, a recent study discovered that the nation's average annual maximum temperature rose by 0.3 to 0.6 °C per decade between 1985 and 2018 (Ware et al., 2022). Similarly, from 1951 to 2006, the minimum temperature increased by 0.37 °C every ten years (Bogale & Tolossa, 2021). Another aspect of climate variability is the fluctuation in rainfall intensity and amount over time and space. The central, southwestern, and southern regions of the country experienced a 15–20% decrease in rainfall in JJAS and FMAM (Belay et al., 2019). These factors had an impact on people's livelihoods, food security, health, and well-being, among other socioeconomic aspects (Belay et al., 2019). Most countries, including Ethiopia and Africa, were heavily affected by the weather and climatic extremes, and this contributed to reduced agricultural productivity, hydrology, ecology, and food insecurity (Zeleke et al., 2023).

Climate variability and change particularly rising temperatures and erratic rainfall, posed serious challenges to rain-fed agriculture and smallholder farmers in Ethiopia, whose livelihoods were highly climate-sensitive and characterized by low adaptive capacity (Kerebo et al., 2024). Although numerous studies reported increasing temperature trends, there was no clear consensus on rainfall patterns, with findings showing both increasing and decreasing trends across different regions and seasons (Dawit et al., 2019; Mohammed et al., 2019 ; Intergovernmental Panel on Climate Change (IPCC), 2013) This inconsistency created uncertainty in understanding local climate behavior. Moreover, most existing studies were conducted at broader spatial scales which failed to capture localized spatiotemporal variability critical for agricultural planning and adaptation. As a result, there was a knowledge gap in location-specific climate variability and trends, particularly at the regional level, such as in CERS. Without clear, localized climate information, it would be difficult to design effective adaptation strategies to reduce vulnerability and sustain agricultural productivity. Therefore, a detailed assessment of spatiotemporal variability and trends of temperature and rainfall at the local scale is essential.

Precipitation variability in the region was notably high, particularly during the FMAM season. Several studies showed that FMAM rainfall exhibited strong inter-annual fluctuations, often associated with a high coefficient of variation (CV), indicating unreliable and erratic rainfall patterns. In contrast, JJAS rainfall, although relatively more stable, still demonstrated considerable variability in terms of onset, cessation, and distribution within the season (Kerebo et al., 2024 ; Moloro, 2018).

Temperature variability in the CERS showed significant temporal and spatial differences. Over recent decades, both minimum and maximum temperatures have exhibited a consistent increasing trend (Kerebo et al., 2024). These climate variations had a direct effect on crop yields, water availability, and agricultural outputs. Despite mounting worries, there is still a lack of comprehensive studies that analyze the region's long-term patterns and trends of temperature and precipitation. This region is one of the vulnerable regions experiencing climate change and variability as well as land degradation (Dendir & Simane, 2019).

The objective of this research was to examine the spatiotemporal variability of precipitation and temperature in CERS using high-resolution gridded data covering 2,500 grid points throughout the entire region at a resolution of 0.05° longitude and latitude. The study also investigated the correlation between regional rainfall and SST. The analysis covered precipitation and temperature data from 1981 to 2023, employing methods such as Standardized Anomaly Index (SAI), Mann-Kendal (MK) trend tests, and the Empirical Orthogonal Function (EOF). The SAI was useful for identifying and comparing climate variability and anomalies over time. The MK trend test was a non-parametric and robust method for detecting monotonic trends in climatic time series, without requiring a normal distribution. The EOF analysis is effective in extracting dominant spatial and temporal patterns of variability from complex climate datasets. Composite analysis was applied to identify the average atmospheric or rainfall patterns associated with specific climate conditions such as El Niño and La Nña events. The analysis was performed by averaging selected years that represent these phases. This helps to highlight consistent signals and anomalies linked to large-scale climate phenomena. On the other hand, correlation analysis was used to quantify the strength and direction of relationships between variables such as sea surface temperature anomalies and rainfall variability. It enabled the identification of statistically significant teleconnections and improved the understanding of how large-scale ocean–atmosphere interactions influenced seasonal rainfall patterns over Ethiopia. Therefore, understanding long-term trends and varia-

tions in seasonal and annual rainfall at a regional level was crucial for developing effective adaptation strategies (Mulugeta et al., 2019).

2 MATERIALS AND METHODS

2.1 Overview of the Study Area

This study focused on CERS, situated at the southern part of Addis Ababa. The area included five administrative zones and one special district (Woreda). Geographically, it is located between 7º4′0′′N Latitude and 38º0′0′′E Longitude (Figure 1). The region is one of Ethiopia's twelve regional states formed recently. This area has a bimodal rainfall regime known locally as FMAM (the short rainy season) and JJAS (the main rainy season) (Worku & Gayler, 2024a).Owing to the mild climate and mostly rolling landscape, the region is very well-suited for agricultural production and human habitation (Yirga, 2021). The mean annual rainfall ranges 955.8mm to 2400mm (Bewket et al., 2024). It is influenced by the movements of the inter-tropical convergence zone as well as the formation of the tropical easterly Jet Stream. The generalized mean minimum temperature is 10.35^{0}C while the mean maximum temperature is 22^{0}C.

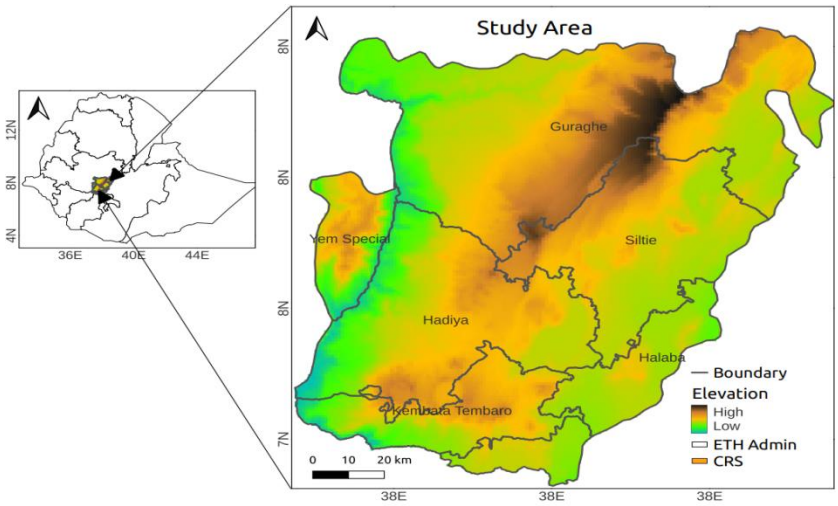

Figure 1. Location of the study area showing elevation (DEM) of the Central Ethiopia Regional State

2.2 Data Description

To investigate the spatial and temporal characteristics of precipitation and temperature in the CERS, the study utilized monthly precipitation data collected from Climate Hazards Center CHIRPS dataset (Funk et al., 2015) over the past 43 years. CHIRPS v2 was a high-resolution satellite-based rainfall estimates and gauge rain dataset (Funk et al., 2015). It was developed

to support climate and weather research particularly in regions with limited ground-based observations. It was developed by the University of California, Santa Barbara Climate Hazards Center. It provides precipitation estimates from 1981 to the present at a spatial resolution of 0.05° (~5 km)(Anose et al., 2021). CHIRPS v2 is a combined dataset that includes observed station data from the Ethiopian Meteorological Institute National Network as well as estimates of satellite data provided by the European Organization for the Use of Meteorological Satellites and the United States National Aeronautics and Space Administration (NASA) (Dinku et al., 2013). CHIRPS enhances data quality and fills spatial and temporal gaps of observation data (Dinku et al., 2013; Esayas et al., 2018). CHIRPS provide compressive spatial coverage and reliable rainfall estimates. Therefore, we preferred to use this gridded data set.
Another data on monthly minimum, mean, and maximum temperatures for the equivalent timeframe were obtained from the Climate Research Unit (CRU-TS4.08) edition of the University of East Anglia. The CRU-TS4.8 gridded data has a resolution of 0.5° longitude by 0.5° latitude (Tate et al., 2001).This is regularly updated from the ground observation of station data. The gridded data was re-gridded by using bilinear interpolation to obtain the same grid resolution with CHIRPS data of rainfall.

In addition, these monthly global sea surface temperature data at a horizontal resolution of 1°X 1° were obtained from the Met Office Hadley Centre. This dataset provided a long-term, quality-controlled record of SST, widely used for climate variability and teleconnection studies (Rayner et al., 2003).

To capture large-scale ocean–atmosphere interactions, this study also incorporated the El Niño–Southern Oscillation (ENSO) and the Indian Ocean Dipole (IOD) indices. ENSO variability quantified using the Oceanic Niño Index (ONI) was obtained from National Oceanic and Atmospheric Administration (NOAA, 2023). The ONI was defined as the 3-month running mean of SST anomalies in the Niño 3.4 region (5°N–5°S, 120°–170°W), and it was commonly used to classify El Niño and La Niña events, with thresholds of ±0.5°C sustained for at least five consecutive overlapping seasons. El Niño referred to the warm phase of ENSO during which sea surface temperatures in the central and eastern tropical Pacific Ocean became significantly warmer than average. This disrupts normal atmospheric circulation and was often associated with reduced rainfall and drought conditions in parts of East Africa including Ethiopia (NOAA, 2023; Clem et al., 2024). La Niña is the cool phase of ENSO characterized

by cooler-than-average sea surface temperatures in the same region. It typically strengthens normal circulation patterns and was often linked to above-average rainfall in parts of East Africa (NOAA, 2023).

Similarly, the IOD was characterized by the Dipole Mode Index (DMI) which represented the SST anomaly difference between the western (50°E–70°E, 10°S–10°N) and southeastern (90°E–110°E, 10°S–0°) equatorial Indian Ocean (Saji & Vinayachandran, 1999). Positive IOD events were associated with warmer SSTs in the western Indian Ocean and cooler conditions in the eastern part while negative IOD events exhibited the opposite pattern. These indices were used to examine the influence of large-scale SST variability on rainfall patterns in the study area.

2.3 Methodology

For this study, the MK trend test, SAI, EOF, correlation, and composite analysis were used to understand trends and behaviors of temperature and precipitation in the CERS for the period of the last 43 years. The distribution of CERS precipitation and temperature was described using descriptive statistics such as skewness, kurtosis, standard deviation, variance, median, and mean (see Tables 1, 2, and 4).

2.3.1 Trend Analysis

We computed the trend test using the MK trend test (Weldegerima et al., 2018; Mann, 1945). Since it is a non-parametric trend test and is less impacted by outliers, it does not assume the Normal distribution of data. The MK trend test is well-established as being quite powerful in detecting trends. This methodology is of great use in all trend detection analyses (Alexander & Arblaster, 2009; Kizza et al., 2009). Equations (1) to (2) are the mathematical formulas used to compute Mann-Kendall statistics (S) and standardized test statistics Z.

$$S = \sum_{i=1}^{N-1} \sum_{j=i+1}^{N} sgn(x_j - x_i) \qquad \text{Eq. 1}$$

With N representing the data set's length, x_i and x_j are the data values in the time series at time steps I and j (j > i), respectively, and sign (x_i and x_j).

$$sgn(\theta) = \begin{cases} +1 if (x_j - x_i) > 0 \\ 0 if (x_j - x_i) = 0 \\ -1 (x_j - x_i) < 0 \end{cases} \qquad \text{Eq. 2}$$

Where: assuming $(x_j - x_i) = \theta$and the values sign (θ) It'll be calculated as the number of data points if the data set is independently and identically distributed, or the signum working. S has a mean of zero, and its variance can be computed using:

$$V(S) = \frac{1}{18}\left[n(n-1)(2n+5) - \sum_{i=1}^{g} t_i(t_i-1)\,(2t_i+5)\right] \qquad \text{Eq. 3}$$

Where g is the number of tied groups (sample data with the same value) in the time series and n is the length of the data set. The sample size (n > 10) is bigger than 10.

$$Z_s = \begin{cases} \frac{S-1}{\sqrt{Var(S)}}, S > 0 \\ 0, S = 0 \\ \frac{S+1}{\sqrt{Var(S)}}, S < 0 \end{cases} \qquad \text{Eq. 4}$$

The standard statistical test is called Z_s. *The* Z_s value was calculated to assess the trend variation's statistical significance level. At 0.05 level of significance, a negative MK statistic (Z < -1.96) showed a substantial decreasing trend while a positive MK statistic (Z > 1.96) showed a significant increasing trend.

Sen's slope estimator was used to predict the magnitude of the Mann-Kendall trend (Sen, 1968). The change per unit of time was computed with the use of this non-parametric technique. This approach assumes that the time series has a linear trend. For each pair of data x, the slope (Ti) is calculated as follows.

$$T_i = \frac{x_k - x_j}{k-j}, j \neq k \qquad \text{Eq. 5}$$

Where: x_j *and* x_k Represent the data values for times k and j, respectively. There will be N = n (n – 1)/2 if the time series has n values (x_j). The median slope of N values of T_i is, therefore, Sen's slope estimator, and overall slope estimator Q_i is calculated as follows:

When N is an odd observation:

$$Q_i = T_{(N+1)/2} \qquad \text{Eq. 6}$$

Or

When N is even observation:

$$Q_i = \frac{1}{2}\left(T_{N/2} + T_{(N+2)/2}\right) \qquad \text{Eq. 7}$$

The slope of the trend line indicates the rate at which either temperature or precipitation has changed over the time (Yi & Zhong-Wei, 2009). To test if the trend was significant, the p-

value was calculated. The p value gives the probability of observing the trend purely by random chance. It is generally accepted that if the p-value is less than 0.05, then the trend is considered statistically significant.

2.3.2 Variability Analysis

2.3.3 Empirical Orthogonal Function

The EOF has been employed in meteorological studies since the 1940s. Mostly, the method is used to explain the variance-covariance of the data by using many modes of variability (Yosef et al., 2017; Chidean et al., 2020). It is a PCA that operates on the spatiotemporal matrix (Biau et al., 1999). EOF is a powerful technique commonly used in spatial and time series analysis to illustrate dominant geographical patterns in multivariate datasets (Roundy, 2015; Joyce, 2002; Hannachi et al., 2023). (Zeleke et al., 2013) provided a useful article that illustrated how to use the traditional EOF method for analyzing climate data. Since the period JJAS and FMAM were wet seasons in the region, the EOF method was employed to attain this objective of the study. Within the research area, this approach allowed for the identification of localized patterns and hotspots of climate variability (Zeleke et al., 2013). The EOF analysis can be expressed as:

$$Z(x,y,t) = \sum_{K=1}^{N} PC(t) * EOF(x,y) \qquad \text{Eq. 8}$$

EOF (x, y) represents the spatial structure with respect to the temporal variance of Z, where Z (x, y, t) represents the function in space (x, y) and at time (t). PC(t) is an essential component in explaining how the amplitude of each EOF changes over time.

The positive and negative anomalies of rainfall and temperature variation in the region were computed using the Standardized Anomaly Index used for identifying dry and wet years (Alemayehu & Bewket, 2017a). Mathematically it is calculated by equation (eq.9):

2.3.4 Standardized Anomaly Index

The Standardized Anomaly Index (SAI) is a statistical measure used to show how much a climate variable (like rainfall or temperature) deviates from its long-term average.

Formula

$$SAI = \frac{x-\overline{x}}{\sigma} \qquad \text{Eq. 9}$$

The mean and standard deviation are denoted by $\bar{x}$ and σ, respectively, where x represents the temperature or rainfall data. Other statistical analysis and computations were done by using MS Excel, RStudio, Python, and Climate Data Operator (CDO) software.

2.3.5 Correlation Analyses

In order to investigate the drivers of rainfall variability in CERS, we used correlation analysis of precipitation with SSTs. The direction and intensity of correlations between variables were evaluated using Pearson's correlation coefficient (r) (Wilks, 2011). Large-scale atmospheric circulations are known to be influenced by slowly changing processes such as variations in SST which can offer predictions on seasonal time frames (Korecha & Barnston, 2007). The correlation analysis of JJAS and FMAM of PCs shown in (Figure 7-11) was correlated with global SST. The null hypothesis, which assumes the absence of relationship between rainfall and large-scale variables, was used in the correlation study. A statistical significance level of 95% or α 0.05 was utilized to interpret the significance of the correlations using Pearson's correlation analysis.

$$r = \frac{\sum[(X_i - \bar{X})\,(Y_i - \bar{Y})]}{\sqrt{[(X_i - \bar{X})^2\ \sum(Y_i - \bar{Y})^2]}} \qquad \text{Eq. 10}$$

Where $\bar{X}$ and $\bar{Y}$ are the means of the corresponding variables, and X_i and Y_i are individual observations. Relationships between dependent and independent variables were investigated using linear regression analysis: Y is the dependent variable, X is the independent variable, β_0 is the y-intercept, β_1 is the slope, and ε is the error term in the formula $Y = \beta_0 + \beta_1 X + \varepsilon$.

2.3.6 Composite Analysis

Composite Analysis is a method used to identify typical patterns by averaging data from multiple events that share a common condition. To better understand the connections between various events, composite analysis was performed in addition to correlation analysis. The composite study for the JJAS and FMAM rainfall of CERS spatial scale was conducted using ENSO and IOD years. El Niño and La Niña years and their intensities were used to determine the positive and negative ENSO events. The negative and positive index of ENSO was derived from La Niña and El Niño years and their intensities. ONI definitions of events were used to categorize La Niña events, with categories including weak, moderate, and strong. Similarly, for El Niño events, the categories were weak, moderate, strong, and very strong.

3 RESULTS AND DISCUSSION

3.1 Seasonal and monthly precipitation

The geographical location of CERS is characterized by a tropical climate with significant climate variability. Figure 2a shows that JJAS contributes more than half of the annual rainfall (57.7%). FMAM is the second-largest rainy season, contributing 32.0% of the annual rainfall (Figure 2b) and ONDJ contributes 10.7% of the annual rainfall (Figure 2c). This study was comparable with the findings of Senbeta et al.'s (2024) study in which it was reported that JJAS season had similar statistical values of precipitation. On the other hand, the lowest amount was recorded in the ONDJ season. The total annual mean precipitation in CERS was 1154.25 mm. The northwest and the western pocket area of CERS received more precipitation in the JJAS season, which was consistent with a study by (Senbeta et al., 2024), and it was dominated by Meher livelihood.

Most of the zones received an amount greater than 140 mm of rain during JJAS. However, the eastern part of the region received less precipitation in JJAS and ONDJ seasons than in FMAM. The precipitation map for FMAM (Figure. 2b) revealed a pronounced increase in precipitation from north to south, except for some western part of the region. In ONDJ most parts of the region received below 60mm of precipitation; however, both FMAM and ONDJ seasons experienced precipitation exceeding ~120 mm in the southern part of the region.

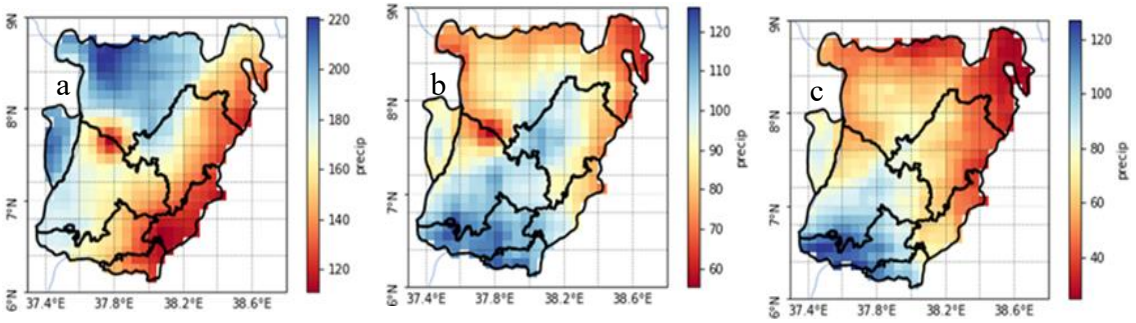

Figure. 2. Climatology of seasonal precipitation (mm) JJAS (a), FMAM (b), and ONDJ(c) in CERS

Figure b shows that July and August had the highest monthly precipitation concentrations. For instance, average precipitation of 192 mm in July and 188 mm in August contributed the most to the annual precipitation budget (16.61% and 16.27%, respectively), followed by September (11.03%) and June (11.38%). Similarly, the average precipitation in January, February, March, April, May, October, November and December were 24 mm, 38 mm, 87 mm,

115 mm, 128 mm, 67mm, 19mm, and 14mm, respectively. January had the least monthly percentile contributions.

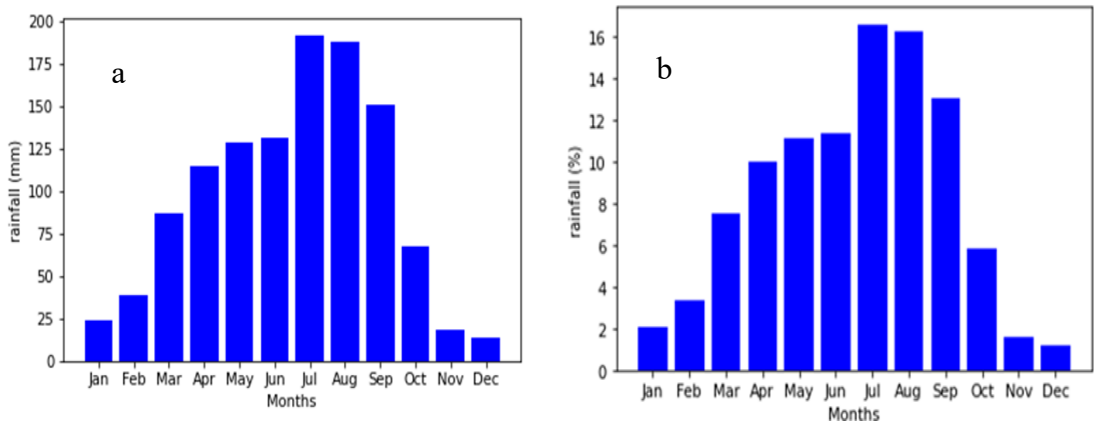

Figure 3. Annual cycle (mm) (a) and the percentage contribution of monthly mean precipitation (mm) (b) in CERS.

As indicated in Table 1, JJAS, ONDJ, and FMAM had mean seasonal rainfall climatology of 166.47 mm, 31.0 mm, and 92.24 mm, with standard deviations of 16.17, 13.21, and 21.28, respectively. During the study period, FMAM had the highest seasonal variance of 453 mm which was consistent with other studies and indicated that the FMAM season in Ethiopia was a highly variable short rainfall season (Abebe et al., 2022; Worku & Gayler, 2024b). Regarding trends across all seasons, there was a non-significant (p-value > 0.05) increase in precipitation, which aligned with A. Belay et al. 2021, who reported a non-significant increase in rainfall in southern Ethiopia. Conversely, Worku and Gayler (2024a) reported an increasing trend in seasonal rainfall in the Gurage Zone during the JJAS season. This suggested that the length and quality of rainfall data_ geographical locations, variations in the data, or lack of ground stations to cover a large area_ were the reasons for the uncertain rainfall trend in Ethiopia (Ahmed et al., 2024).

Table 1 Descriptive Statistics of seasonal precipitation(mm).

Seasons	p-value	slope	mean	median	Variance	Std.	Skewness	Kurtosis	Range
JJAS	0.43	0.18	166.47	167.51	261.36	16.17	-0.19	-0.46	63.98
ONDJ	0.07	0.28	31.00	30.66	174.38	13.21	0.83	1.09	63.55
FMAM	0.93	0.031	92.24	90.65	452.88	21.28	0.03	-1.01	74.91

Table *2*: The MK test result showed that the analysis of monthly trends showed significant increases in precipitation during September (p = 0.036**,** slope = 0.67) and November (p = 0.001**,** slope = 0.34), indicating a tendency for wetter conditions in these months over the

study period. The increase in rainfall during November aligned with the findings of (Senbeta et al., 2024b). Other months did not exhibit statistically significant trends ($p > 0.05$). Meanwhile, the variance and standard deviation (Std.) highlighted the variability of precipitation. May exhibited the highest variability (Var. = 2226.79**,** Std. = 47.19 mm), reflecting a broader range of precipitation values. Conversely, December showed the least variability (Var. = 137.53**,** Std. = 11.73 mm). Regarding central tendency, the mean and median precipitation values highlighted distinct seasonal differences. July recorded the highest mean precipitation (191.76 mm) consistent with its status as a peak rainy month while December had the lowest mean (13.57 mm) reflecting the dry season. Median values were generally close to the means, implying symmetrical distributions for most months.

Table 2 Descriptive Statistics of monthly precipitation.

Months	**p-value**	**slope**	**mean**	**media**	**Var.**	**Std.**	**Kurtosis**	**Skewness**	**Range**
Jan	0.70	-0.02	24.30	17.82	243.13	15.59	0.3	1.01	62.55
Feb	0.32	-0.25	38.45	30.43	746.45	27.32	1.19	1.59	137.52
Mar	0.41	-0.52	87.16	75.08	1941.97	44.07	0.25	0.83	171.81
Apr	0.41	0.39	115.05	119.66	1565.65	39.57	-0.01	0.03	181.08
May	0.17	0.91	128.30	126.24	2226.79	47.19	-0.08	0.24	204.91
June	0.53	0.21	131.33	133.02	793.44	28.17	-0.22	-0.01	124.91
July	0.60	-0.24	191.76	193.95	1020.61	31.95	-0.69	-0.17	119.99
Aug	0.86	-0.04	187.81	183.78	633.70	25.17	-0.23	-0.12	108.19
Sep	0.036	0.67	150.37	149.25	817.19	28.59	-0.19	0.67	106.29
Oct	0.13	0.76	67.49	66.05	1627.31	40.34	0.53	0.75	176.26
Nov	0.001	0.34	18.63	12.16	198.75	14.10	1.11	1.39	54.50
Dec	0.66	-0.02	13.57	9.12	137.53	11.73	3.57	1.97	47.50

As shown in Figure 4 below, July and August received the highest amount of rainfall in the northwest part of the study domain. Throughout the research period, December, January, and November had the lowest rainfall distribution compared to other months. September and March had high spatial coverage of rainfall; in contrast, the southern part of the region experienced little to no rainfall in June, July, and August *(Figure 4)*. The temporal and spatial varia-

bility of the precipitation was examined by the empirical orthogonal function. (Hannachi et al., 2007) had a detailed approach and provided further details and mathematical formulas.

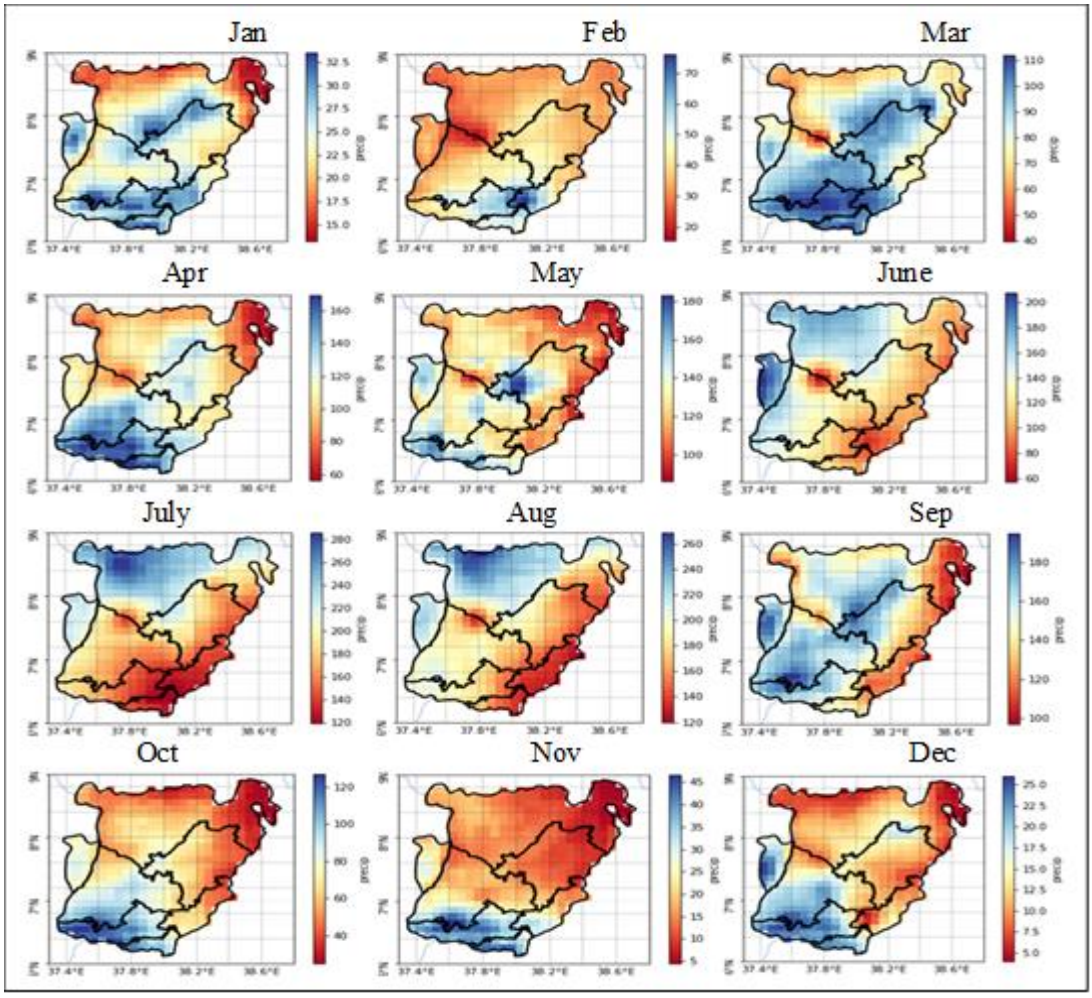

Figure 4. CHIRPS monthly rainfall (mm) climatology over CERS from 1981-2023

Figure depicts the variation of precipitation across space throughout JJAS season with three significant modes highlighted: EOF1, EOF2, and EOF3 explaining 63.8%, 13.5%, and 6.93% of the total variance, respectively. This mode collectively accounted for 84.23% of the rainfall variability. The first mode of EOF, EOF1 showed a consistent spatial pattern except the southwest, central, and eastern pocket area of the region accounting for 63.80% of the total rainfall variability. This indicates that the central and eastern pocket areas are more likely to experience wet conditions during the JJAS season. 13.50% of the variance was explained by the second EOF mode which exhibited a clear north-south dipole pattern with a high variability in the south and the weakest variation in the North West (*Figure* b). The third mode (*Figure* c) explained 6.93% variance, showing a positive loading in the west and a negative loading in the east. It exhibited the weakest variability in the northeastern part of the region. The first three EOFs adequately described the spatial pattern because they were primarily

linked to a broad atmospheric circulation that affected weather patterns (Ehsan et al., 2021). The seasonal precipitation differences from year to year are examined in *Figure* d. Wet (flood) and dry (drought) years were identified using a threshold of ±1 standard deviation from the long-term mean. Years with values greater than one standard deviation above the mean were classified as wet years, whereas years with values lower than one standard deviation below the mean were classified as dry years. The wet years for PC1 with an amplitude greater > +1 standard deviation were 1988, 1994, 1996, 1998, 2007, 2008, 2012, and 2013, and 2019. However, the dry years were 1981, 1982, 1987, 1997, 2009, 2015, and 2016 having an amplitude < −1 standard deviation. The PC2 displayed wet conditions in 2002, 2007, 2013, 2014, 2015, and 2019 whereas the dry conditions were in 1990, 1993, 1994, 1998, 2009, 2011, and 2023. Similarly, the PC3 had the wet years 1985, 1986, 1990, 1991, 1992, 1995, 1998, and 2002 and dry 1996, 2008, 2011, 2016, 2020, and 2023.

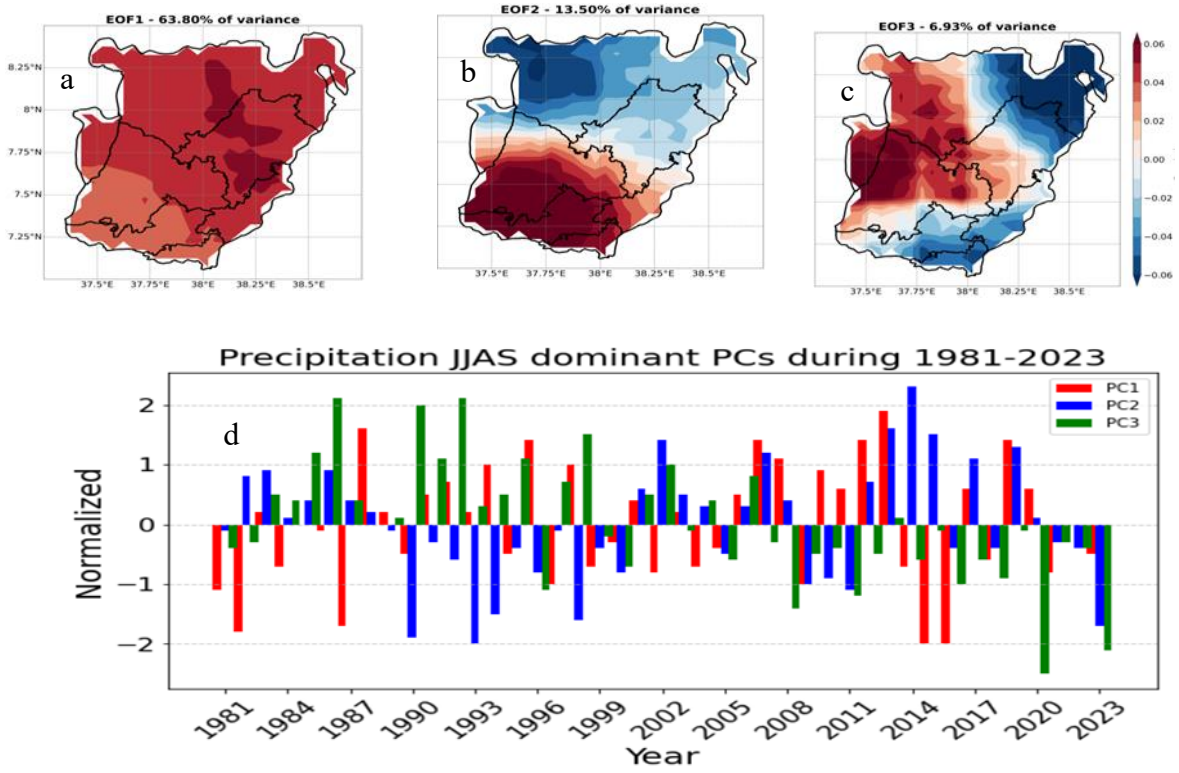

Figure 5 shows the spatial variation of precipitation using EOF1(a), EOF2(b) and EOF3(c) for JJAS, together with the main components PCs that illustrate the associated temporal variability Figure 5(d).

Similarly,
illustrates the spatial variations of FMAM seasons, and precipitation while
d shows a temporal time series. During this season, the first, second, and third EOF of precipitation explained 82.13%, 6.52%, and 3.51% of variance, respectively. Throughout the whole study area domain, the EOF1 displayed positive loadings, which showed a

homogenous pattern indicating the region had the same variability. In EOF2, the large precipitation variance happened in the western part of the region, whereas less precipitation variability was implied by an area with negative loadings in the eastern part. Similarly, the greater precipitation variability was indicated in the southern part of the region in EOF3. The PC1 demonstrated that the time series contained ten wet years as 1983, 1987, 1990, 1993, 1996, 2010, 2014, 2016, 2018, and 2023 and eight dry years: 1984, 1988, 1999, 2000, 2008, 2009, 2012 and 2022. PC2 had seven wet years 1992, 1993, 1994, 1996, 1997, 2014, and 2019. The five dry years were 1982, 1987, 2010, 2012, and 2016. The PC3 of EOF3 also had six wet years: 1987, 1998, 2013, 2014, 2018, and 2022 and six dry years: 1989, 1993, 1995, 1996, 2016, and 2023. In general, wet years outnumbered dry years in JJAS and FMAM seasons. This indicated flooding and availability of water within the region.

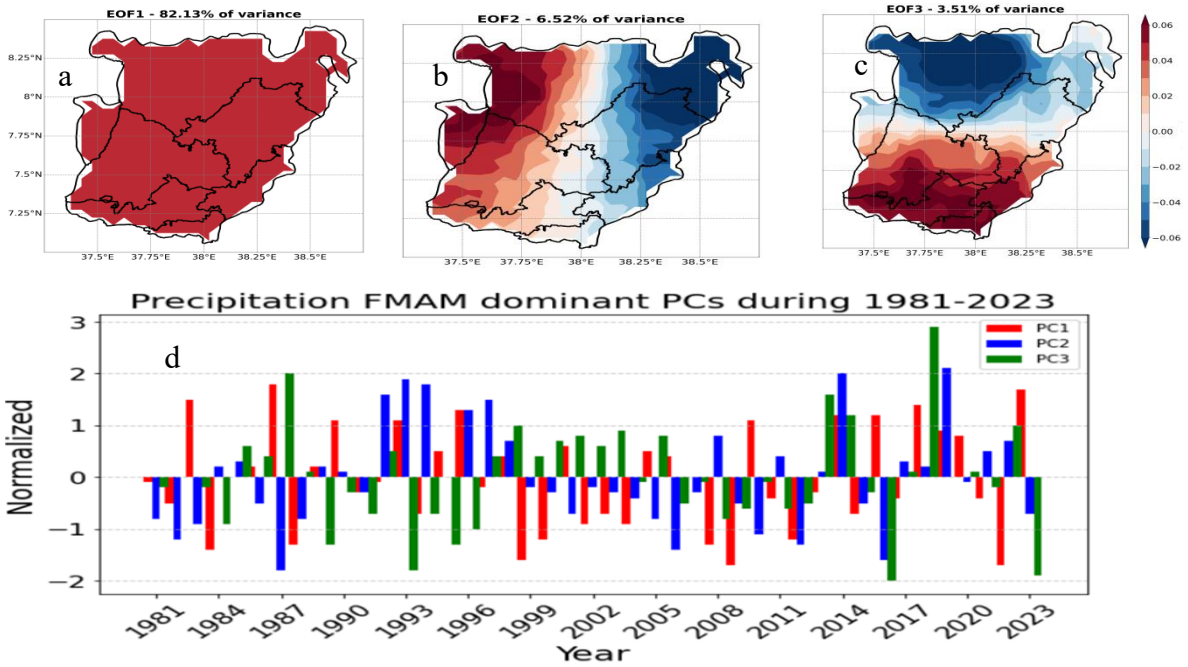

Figure 6 shows the spatial variation of precipitation using EOF1(a), EOF2(b) and EOF3(c) for FMAM, together with the main components PCs that illustrate the associated temporal variability Figure 6(d).

3.2 Drivers of Rainfall Variability Based on Principal components (PCs)

3.2.1 Correlation Analysis

To identify the drivers of rainfall variation, the long-term and spatial scales of rainfall in central Ethiopia were investigated using correlation analysis with sea surface temperature and principal components. Changes in sea surface temperature could influence large-scale atmospheric circulation and provide seasonal predictability. As shown in Table 3, the

correlation between rainfall variability and oceanic SST anomalies highlighted the vulnerability of the climate system in central Ethiopia to global ocean changes.

Table 3 summarizes the temporal behavior and variance explained by the top EOF modes and their SST relationship.

Season	Mode	Variance Explained (%)	Temporal Behavior	Links with SST Drivers
JJAS	PC1	63.80	Interannual fluctuations	Strong positive linkage with western pacific and Eastern Indian Ocean and negative linkage with Central and Eastern Pacific Ocean
	PC2	13.50	Interannual fluctuations	Has a strong positive correlation with Eastern Indian & Pacific Oceans.
	PC3	6.93	Long term trend & Interannual fluctuations	Strong negative linkage with Northern Atlantic Ocean & Positive linkage with Tropical Pacific Ocean
FMAM	PC1	82.13	Interannual fluctuations	Positive linkage with Pacific, Atlantic & Indian Ocean.
	PC2	6.52	Long term trend & Interannual fluctuations	Weak positive linkage with Pacific Ocean and negative linkage with Western Indian Ocean.
	PC3	3.51	Interannual fluctuations	Positive linkage with Atlantic and Indian Ocean

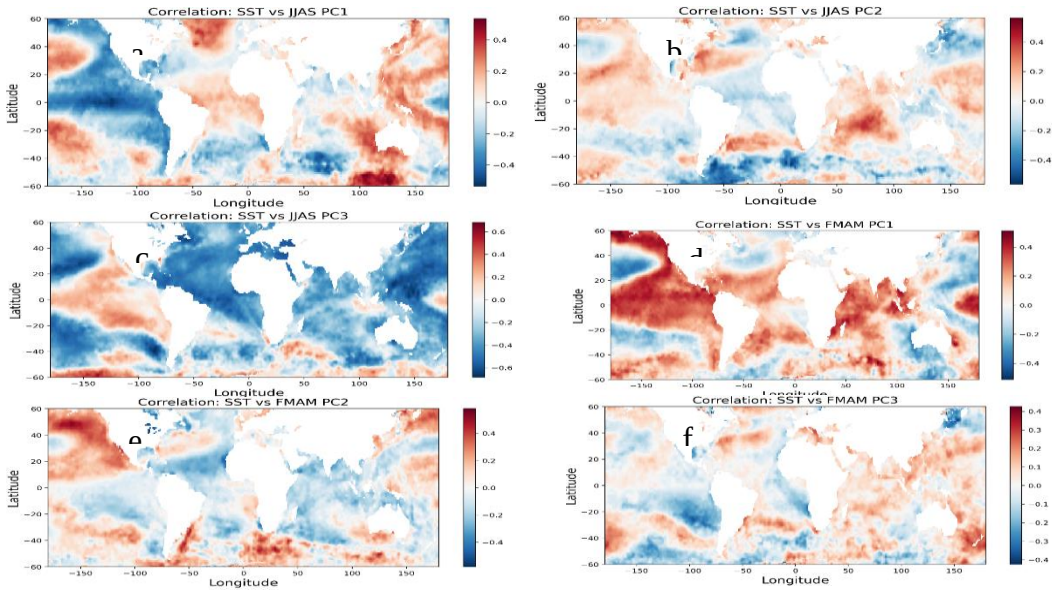

Figure 7 (a-f). Pearson correlation patterns between dominant seasonal rainfall components (PCs) and global sea surface temperature (SST) from 1981 to 2023

3.2.2 Composite Analysis

Figure 8(a-d) presents the composite rainfall anomalies during JJAS under positive and negative Niño 3.4 phases. It also shows the conditions during positive Indian Ocean Dipole (IOD) events. Composite maps of JJAS rainfall are shown for a very strong El Nino year (Figure 8a) and Strong La Niña years (Figure 8b). Very strong El Nino events were associated with drier than normal JJAS rainfall in all parts of CERS. Especially, the southern part was drier than northern part. On the other hand, most of the region had wetter conditions during La Nina occurrences (Figure 8b). These results were consistent with the findings of other scholars (Haile et al., 2021; Montgomery et al., 2013). El Nino and La Nina conditions were generally associated with drier and wetter years in many parts of the country, respectively. The result of the composite map based on IOD presented a mixed image (Figure 8c & d). Positive IOD years were associated with increased JJAS rainfall in the northern and southeastern parts of the region. Negative IOD was associated with weakly dry conditions in most parts of the study area (Figure 8d). Generally speaking, the positive phase of IOD happened during El Nino years, and its negative phase happened during La Nina years (Stuecker et al., 2017). During FMAM, under positive Niño 3.4 (El Niño) conditions, the study area exhibited a dipole rainfall pattern, characterized by enhancing rainfall in the central and northeastern regions and deficit rainfall in the western and southwestern parts. The southern eastern and the central portions of the region showed enhanced rainfall, with anomalies greater than 0.6 – 0.8 mm/day.

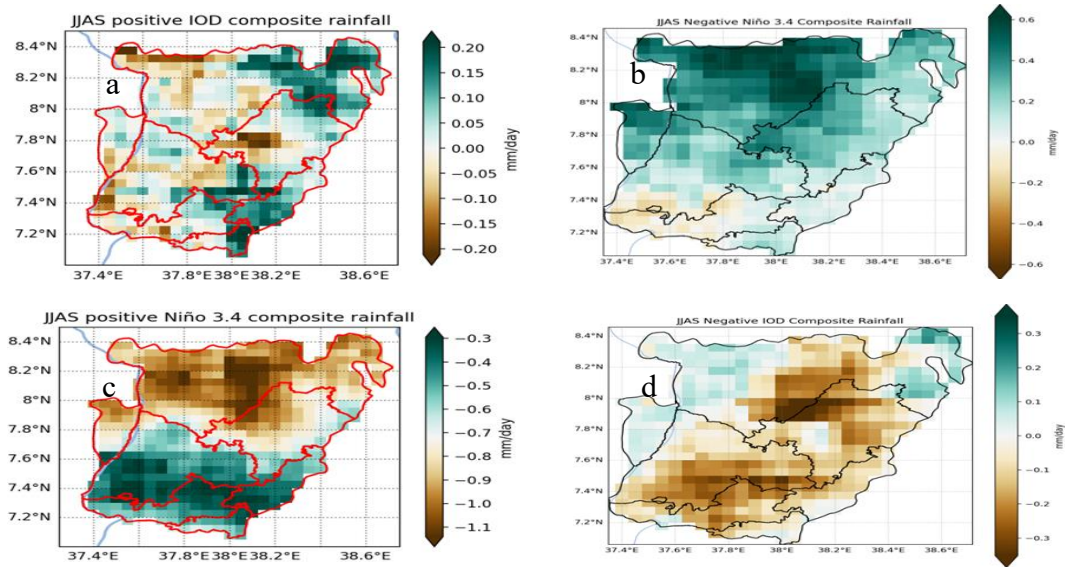

Figure 8(a-d). Composite maps of JJAS rainfall for very strong El Nino and La Nina years (a and b) and for positive (c), negative IOD years (d).

The La Niña phenomenon produced a spatial response opposite to the positive phase. In Figure 9(b), the rainfall deficit predominates the northern and the southern segments of the region, reaching -0.6 to -0.8 mm/day, while rainfall concentration is increased across the western and eastern parts. In Figure 9(c), rainfall is mainly concentrated in northern and western parts of the region, with some area showing higher intensity.

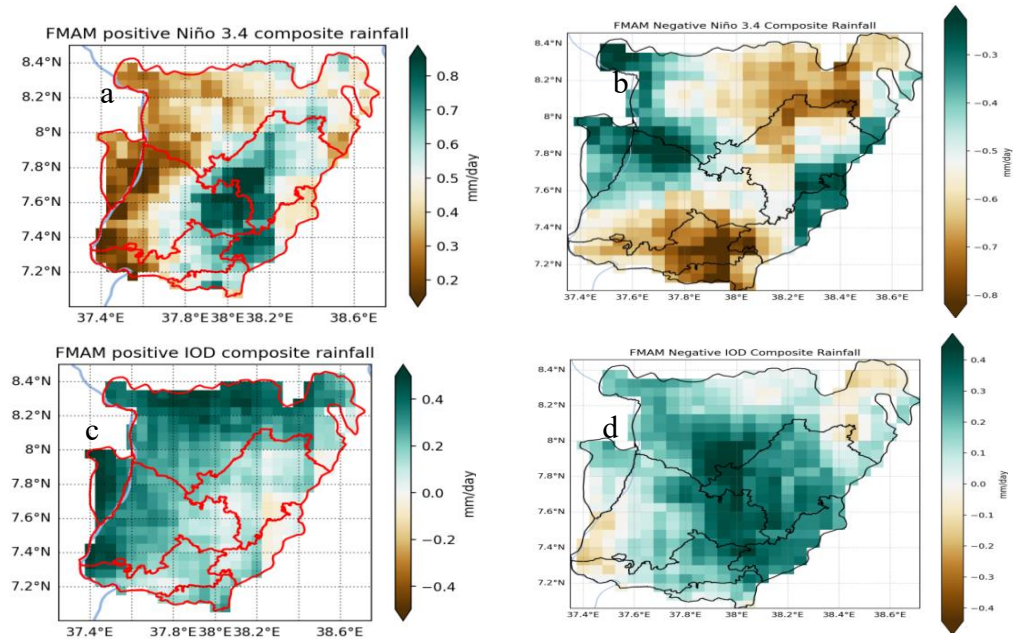

Figure 9(a-d). Composite maps of FMAM rainfall for very strong El Nino years (a and b) and for positive (c), negative IOD years (d).

3.3 Seasonal and Monthly Mean Temperature

The CRU (mean 2m) temperature distribution presented in Figure 10 depicts the spatial mean seasonal minimum, mean, and mean maximum temperature whereas Figure 11 shows the monthly mean temperature of the year from 1981-2023. As illustrated in Figure 10, the average seasonal temperature (tmp) varied between 13°C and 20°C. During the JJAS season, the region experienced relatively lower maximum temperatures. This was similar to the findings of (Worku & Gayler, 2024b). FMAM is the hottest season with a mean maximum temperature of 26.52°C while ONDJ is the lowest with a mean nighttime temperature of 8.82°C (.

Table 4). With regard to precipitation (Figure 2a), the northwest typically experienced greater maximum nighttime temperatures. Diurnal temperature was increasing from north to south.

In Figure 11, the lowest temperature was observed in December with the value of 7.56°C, but February was the hottest month which had the mean warmest temperature of (27.39°C).

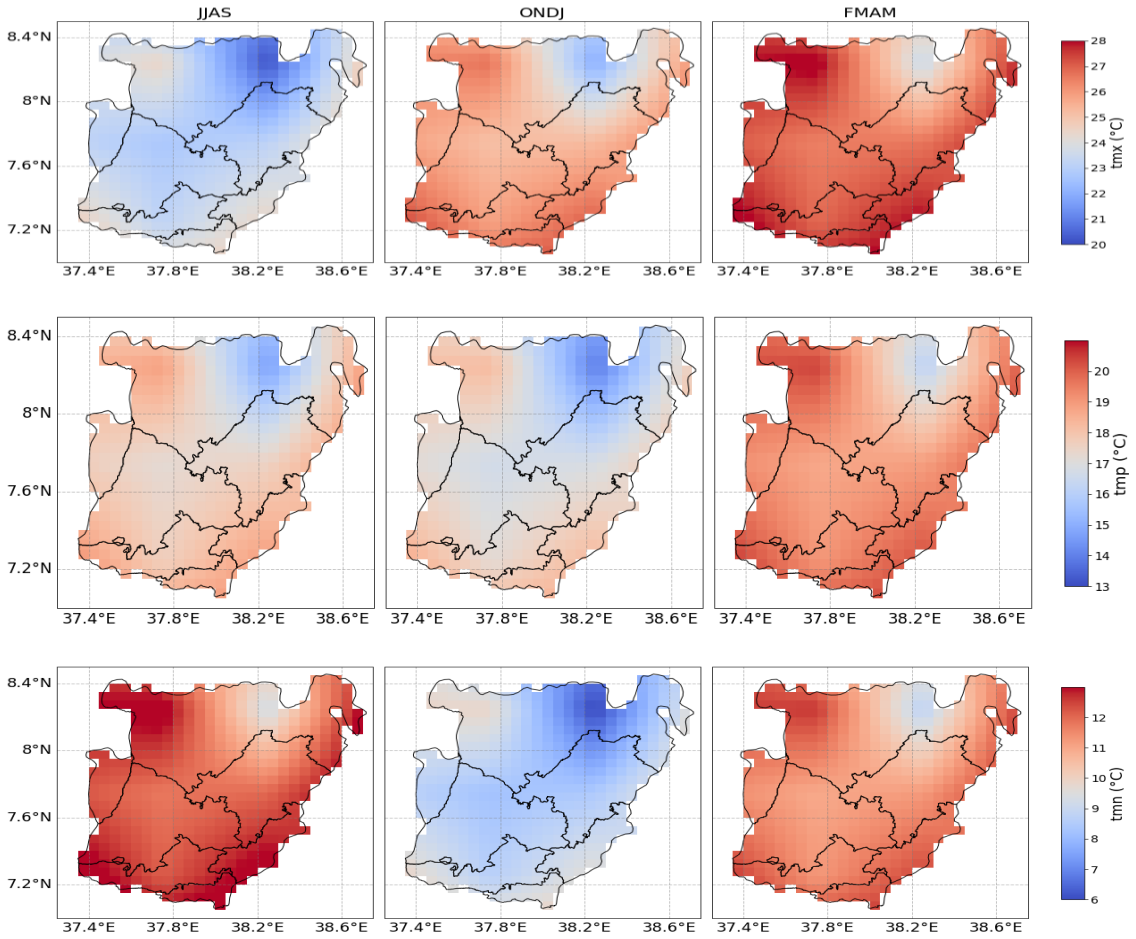

Figure 10. The spatial variation of temperature in the CERS.

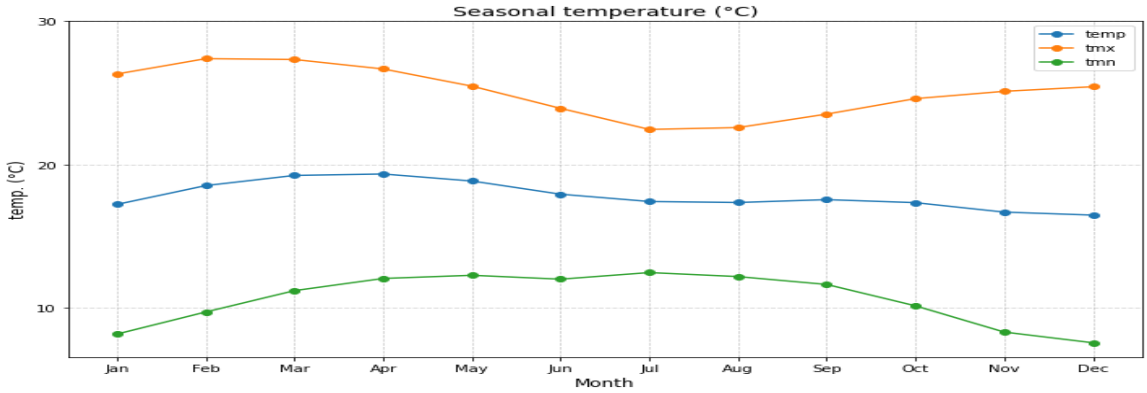

Figure 11. Seasonal temperature cycle in degrees Celsius (°C)

3.4 Temperature Trend

.

Table **4** indicates the analysis of notable temperature trends across the seasons. The JJAS minimum temperature shows a highly significant increasing trend, with a p-value of 0.03. Indicating statistically significant warming. This had a low variance of 0.12 with a standard deviation of 0.35, indicating somewhat consistent temperature with slight left skewness. For the ONDJ season, more statistically significant results were obtained, with a p-value of 0.00. The trend shows a slope of 0.02. The mean minimum temperature is 8.82°C, and the median is 8.7°C. The data also show high variance and a relatively large standard deviation.

A significant increase was observed during both the FMAM and ONDJ seasons, mean temperatures (tmp) show statistically significant results. The p-values of 0.00 indicate very strong increasing trends. The slope is 0.028 for FMAM and 0.025 for ONDJ. ONDJ showed 18.96°C on average while FMAM had a slightly below that, the average temperature is 17.63 °C, giving. The JJAS season also shows an increase of 0.018 compared to the statistical trends. Variance values were consistent and stable within the seasons.

Maximum temperatures (tmx) changed significantly, especially during the FMAM season, with a slope of 0.04 and a p-value of 0.0009. Its mean maximum temperature was 23.22°C. ONDJ also showed a strong trend, having a p-value of 0.00 and a mean of 25.10°C. The FMAM season had a mean maximum temperature of 26.52°C. This outcome was in line with the research results of (Worku & Gayler, 2024b). The variability was highest in the FMAM, showing greater variation in maximum temperatures. Overall, it suggested that it was warmest temperature of all the seasons. A significant change occurred especially during the ONDJ and FMAM periods, consistent with the findings in Ethiopia (Alemayehu & Bewket 2017b; Abara & Budiastuti, 2020; Jury & Funk, 2013).

Table 4 Descriptive statistics of seasonal mean Temperature.

Seasons	slope	p-value	median	mean	Variance	Std.	Kurtosis	Skewness	Range
Mean minimum temperature (tmn) 1981-2023									
JJAS	0.01	0.03	12.1	12.09	0.12	0.35	-0.16	-0.16	1.6
ONDJ	0.02	0.00	8.7	8.82	0.32	0.56	0.04	0.08	2.6
FMAM	0.01	0.06	11.5	11.46	0.42	0.65	0.58	-0.18	3.1
Mean temperature (tmp) 1981-2023									
JJAS	0.018	0.00	17.6	17.63	0.14	0.38	-0.39	0.28	1.50
ONDJ	0.025	0.00	17.04	16.93	0.15	0.39	-0.75	-0.10	1.59
FMAM	0.028	0.00	19.01	18.96	0.28	0.52	-0.15	-0.40	2.31

Maximum temperature (tmx) 1981-2023									
JJAS	0.021	0.0008	23.10	23.22	0.37	0.61	0.27	0.54	2.56
ONDJ	0.028	0.00	25.17	25.10	0.31	0.56	-0.31	-0.49	2.29
FMAM	0.04	0.0009	26.66	26.52	0.76	0.87	-1.08	-0.31	3.31

3.4.1 Anomalies in Annual Mean Temperature

Figure 12(a-c) summarizes the key findings of the yearly anomalies of minimum, mean, and maximum temperatures. The yearly anomalies of minimum temperature, particularly the years between 1981 and 2004, except for 1983, 1987, 1991, 1995, and 1996, showed significant negative anomalies, indicating cooler temperatures. Since late 2005, there has been a record of high positive anomaly which peaked in 2009-2011 and then remained elevated until 2015-2017. In general, the past forty years were marked by both positive and negative anomalies of minimum temperature with a notable increase observed in the later years especially in 2013 and 2016.

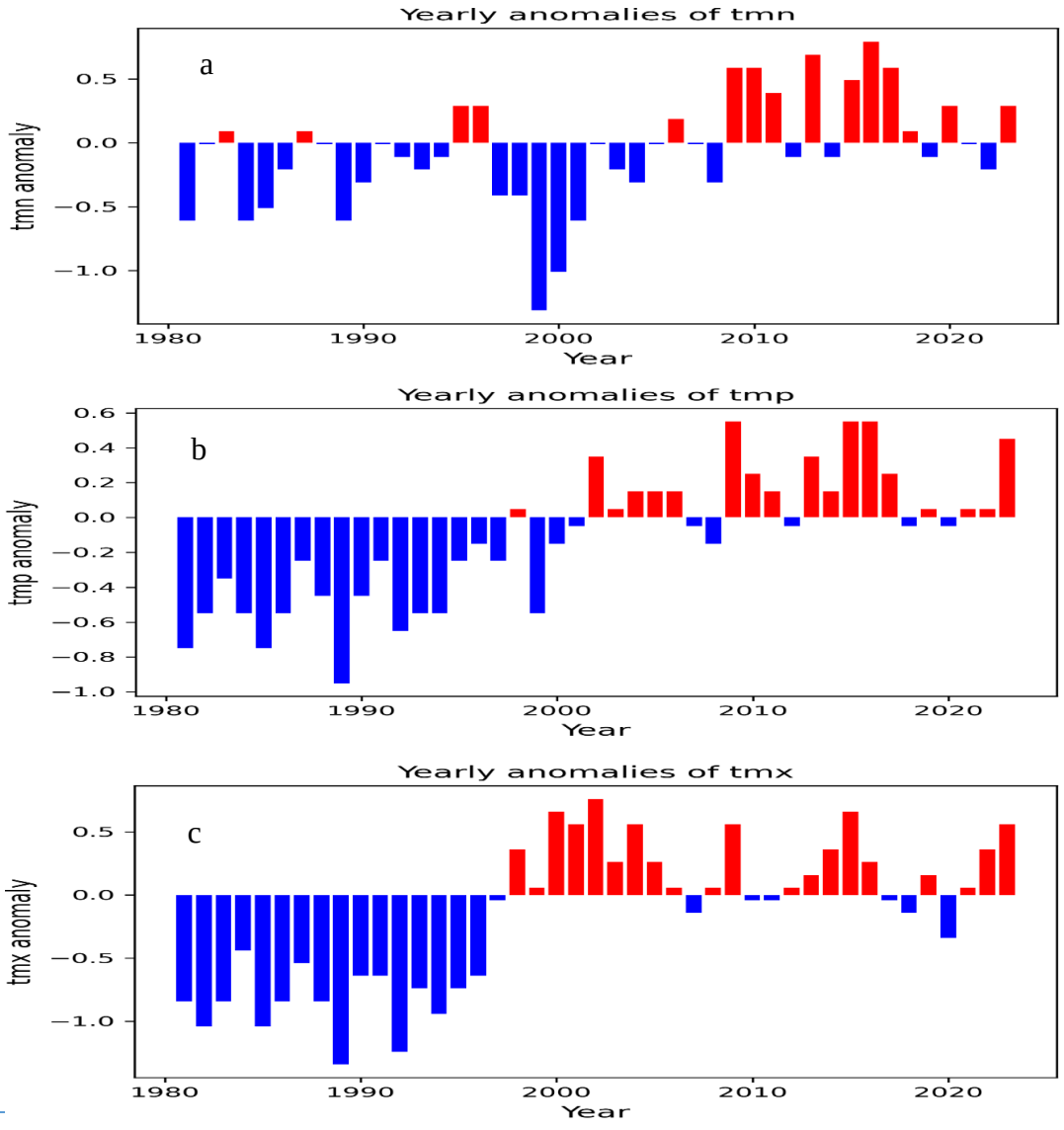

Figure 12(a-c) Standardized anomaly of mean annual temperature calculated from the CRU data set for 1981-2023

The mean temperature presented consistent negative anomalies throughout the 1980s and '90s, indicating cooler than average temperature. Since 2000, there has been a distinct shift toward predominantly positive anomalies indicating a warming trend through the last decade. This finding showed definite evidence to support the idea of a regime shift in climate, namely the cool conditions in the earlier period giving way to warm conditions in more recent times. This was consistent with global patterns of climate change (Jury & Funk, 2013; Belay et al., 2021). The anomalies of maximum temperature from 1981-1997 were negative, suggesting a trend relative to a reference period. The period from the early 2000s showed a significant increase in the frequency and magnitude of positive anomalies, suggesting an upward trend in maximum temperatures. Recent years exhibited a general warming trend. Occasional years still exhibit slight negative anomalies. This indicates the presence of inter-annual climate variability. In general, before the year 2000, air temperature anomalies were consistently negative, but from 2000 onward, there has been a noticeable warming trend.

4 CONCLUSION

This study examined the trends and spatiotemporal variability of temperature and precipitation in the CERS. The results indicated that the region experiences distinct seasonal rainfall patterns, with mean climatological values of 166.17 mm, 31.0 mm, and 92.24 mm for JJAS, ONDJ, and FMAM, respectively. The annual mean precipitation was found to be 1154.25 mm. Among the seasons, JJAS contributed the largest share of annual rainfall (57.7%), followed by FMAM (32%) and ONDJ (10.3%). The spatial distribution of rainfall was strongly influenced by geographic factors, with the northwestern parts of the region receiving higher precipitation during the JJAS season. In contrast, FMAM was characterized by high variability, making it a less reliable rainfall season. Trend analysis revealed no clear increasing pattern in seasonal rainfall; however, statistically significant increasing trends were observed in September and November precipitation. Overall, these findings highlighted the variability and uneven distribution of rainfall in CERS, which had important implications for climate-sensitive sectors particularly rainfed agriculture. EOF analysis highlighted dominant modes of variability in rainfall. For instance, the first mode explained 82.13% of rainfall variability during FMAM, indicating a homogeneous spatial pattern. Similarly, there

was a variance of 63.80% in JJAS season. The correlation analysis between rainfall principal components and global SSTs revealed rainfall variability across the CERS. Overall, major ocean basins such as the Pacific, Indian, and Atlantic Oceans are consistently and meaningfully linked to the principal EOF modes (PC1–PC3).

The largest portion of rainfall variability was explained by PC1 for both the JJAS and FMAM seasons. It showed substantial connections with SSTs in the Pacific and Indian Oceans, suggesting that ENSO-related processes were important drivers. Additional variability pertaining to long-term trends and variations connected to SST anomalies in the Atlantic and Indian Oceans were captured by the two modes (PC2 and PC3). These results highlighted that rainfall variability in Central Ethiopia was not random but reflected coherent teleconnections with global SST patterns, supporting the potential for seasonal predictability.

A significant warming trend was identified across all seasons of minimum, mean, and maximum temperatures. ONDJ and FMAM seasons experienced the most pronounced warming trends, indicating a transition to higher temperatures over the study period. Annual temperature anomalies shifted from cooler years in the 1980s to warmer years in recent decades, consistent with global climate change patterns. Based on the high variability of FMAM rainfall, the dominance of JJAS rainfall, and the spatial unevenness of precipitation, the study recommends targeted risk management strategies such as season-specific agricultural planning, climate-resilient water management, improved climate information, early warning systems, and location-specific adaptation measures.

DATA AVAILABILITY

The data set created during the current study can be obtained from the first author upon request.

ACKNOWLEDGEMENT

I would like to express my deepest gratitude to Ethiopian Meteorology Institute and Arba Minch University, Arba Minch Water Technology Institute, and Water Resource Research Center (WRRC) for providing a grant to conduct this research.

CONFLICT OF INTEREST

No conflicts of interest are disclosed by the authors.

REFERENCE

Abara, M., & Budiastuti, S. (2020). Drought frequency, severity, and duration monitoring based on climate change in southern and southeastern Ethiopia. *IOP Conference Series: Earth and Environmental Science*, *477*(1), 12011.

Alemayehu, A., & Bewket, W. (2017a). Determinants of smallholder farmers' choice of coping and adaptation strategies to climate change and variability in the central highlands of Ethiopia. *Environmental Development*, *24*, 77–85.

Alemayehu, A., & Bewket, W. (2017b). Local spatiotemporal variability and trends in rainfall and temperature in the central highlands of Ethiopia. *Geografiska Annaler: Series A, Physical Geography*, *99*(2), 85–101.

Alexander, L. V, & Arblaster, J. M. (2009). Assessing trends in observed and modelled climate extremes over Australia in relation to future projections. *International Journal of Climatology: A Journal of the Royal Meteorological Society*, *29*(3), 417–435.

Anose, F. A., Beketie, K. T., Terefe Zeleke, T., Yayeh Ayal, D., & Legese Feyisa, G. (2021). Spatio-temporal hydro-climate variability in Omo-Gibe river Basin, Ethiopia. *Climate Services*, *24*, 100277. https://doi.org/https://doi.org/10.1016/j.cliser.2021.100277

Belay, A., Demissie, T., Recha, J. W., Oludhe, C., Osano, P. M., Olaka, L. A., Solomon, D., & Berhane, Z. (2021). Analysis of climate variability and trends in Southern Ethiopia. *Climate*, *9*(6), 1–17. https://doi.org/10.3390/cli9060096

Belay, A. S., Fenta, A. A., Yenehun, A., Nigate, F., Tilahun, S. A., Moges, M. M., Dessie, M., Adgo, E., Nyssen, J., Chen, M., Van Griensven, A., & Walraevens, K. (2019). Evaluation and application of multi-source satellite rainfall product CHIRPS to assess spatio-temporal rainfall variability on data-sparse western margins of Ethiopian highlands. *Remote Sensing*, *11*(22), 1–22. https://doi.org/10.3390/rs11222688

Berihu, T., Chen, W., & Wang, L. (2024). Rainfall variability and its teleconnection with atmospheric circulation anomalies over southern and southeastern region, Ethiopia. *Theoretical and Applied Climatology*, *155*(7), 5819–5834. https://doi.org/10.1007/s00704-024-04956-0

Bewket, W., Tibebe, D., Teferi, E., & Degefu, M. A. (2024). Changes in mean and extreme rainfall indices over a problemscape in central Ethiopia. *Environmental Challenges*, *15*(December 2023), 100883. https://doi.org/10.1016/j.envc.2024.100883

Biau, G., Zorita, E., von Storch, H., & Wackernagel, H. (1999). Estimation of precipitation by kriging in the EOF space of thesea level pressure field. *Journal of Climate*, *12*(4), 1070–1085.

Bogale, G. A., & Tolossa, T. T. (2021). Climate change intensification impacts and challenges of invasive species and adaptation measures in Eastern Ethiopia. *Sustainable Environment*, *7*(1), 1875555. https://doi.org/10.1080/23311843.2021.1875555

Chidean, M. I., Caamaño, A. J., Casanova-Mateo, C., Ramiro-Bargueño, J., & Salcedo-Sanz, S. (2020). Spatio-temporal climate regionalization using a self-organized clustering approach. *Theoretical and Applied Climatology*, *140*, 927–949.

Clem, K. R., Diamond, H. J., Lumpkin, R., & Thoman, R. L. (2024). *STATE OF THE CLIMATE IN 2023 Special Supplement to the*. *105*(8), 277–330. https://doi.org/10.1175/2024BAMSStateoftheClimate.1.

Dawit, M., Halefom, A., Teshome, A., Sisay, E., Shewayirga, B., & Dananto, M. (2019). Changes and variability of precipitation and temperature in the Guna Tana watershed, Upper Blue Nile Basin, Ethiopia. *Modeling Earth Systems and Environment*, *5*(4), 1395–1404. https://doi.org/10.1007/s40808-019-00598-8

Dawson, B., & Spannagle, M. (2008). CLIMATE CHANGE IMPACTS. In *The Complete Guide to Climate Change* (pp. 108–114). Routledge.

Dendir, Z., & Simane, B. (2019). Livelihood vulnerability to climate variability and change in different agroecological zones of Gurage Administrative Zone, Ethiopia. *Progress in Disaster Science*, *3*, 100035.

Dinku, T., Hailemariam, K., Maidment, R., Tarnavsky, E., & Connor, S. (2013). Combined use of satellite estimates and rain gauge observations to generate high-quality historical rainfall time series over Ethiopia. *International Journal of Climatology*, *34*(7), 2489–2504.

Ehsan, M. A., Tippett, M. K., Robertson, A. W., Almazroui, M., Ismail, M., Dinku, T., Acharya, N., Siebert, A., Ahmed, J. S., & Teshome, A. (2021). Seasonal predictability of Ethiopian Kiremt rainfall and forecast skill of ECMWF's SEAS5 model. *Climate Dynamics*, *57*(11), 3075–3091.

Esayas, B., Simane, B., Teferi, E., Ongoma, V., & Tefera, N. (2018). Trends in extreme climate events over three agroecological zones of southern Ethiopia. *Advances in Meteorology*, *2018*(1), 7354157.

Funk, C., Peterson, P., Landsfeld, M., Pedreros, D., Verdin, J., Shukla, S., Husak, G.,

Rowland, J., Harrison, L., & Hoell, A. (2015). The climate hazards infrared precipitation with stations—a new environmental record for monitoring extremes. *Scientific Data*, *2*(1), 1–21.

Haile, B. T., Zeleke, T. T., Beketie, K. T., Ayal, D. Y., & Feyisa, G. L. (2021). Analysis of El Niño Southern Oscillation and its impact on rainfall distribution and productivity of selected cereal crops in Kembata Alaba Tembaro zone. *Climate Services*, *23*, 100254.

Hannachi, A., Finke, K., & Trendafilov, N. (2023). Common EOFs: a tool for multi-model comparison and evaluation. *Climate Dynamics*, *60*(5), 1689–1703.

Hannachi, A., Jolliffe, I. T., & Stephenson, D. B. (2007). Empirical orthogonal functions and related techniques in atmospheric science: A review. *International Journal of Climatology*, *27*(9), 1119–1152.

Intergovernmental Panel on Climate Change (IPCC). (2023). Climate Change 2021 – The Physical Science Basis. In *Climate Change 2021 – The Physical Science Basis*. https://doi.org/10.1017/9781009157896

Joyce, T. M. (2002). One hundred plus years of wintertime climate variability in the eastern United States. *Journal of Climate*, *15*(9), 1076–1086.

Jury, M. R., & Funk, C. (2013). Climatic trends over Ethiopia: Regional signals and drivers. *International Journal of Climatology*, *33*(8), 1924–1935. https://doi.org/10.1002/joc.3560

Kerebo, K. A., Bizuneh, Y. K., Mekonnen, A. G., & Mohammed, Y. (2024). The trends and spatiotemporal variability of temperature and rainfall in Hulbarag district, Silte Zone, Ethiopia. *Heliyon*, *10*(11), e31646. https://doi.org/10.1016/j.heliyon.2024.e31646

Kizza, M., Rodhe, A., Xu, C.-Y., Ntale, H. K., & Halldin, S. (2009). Temporal rainfall variability in the Lake Victoria Basin in East Africa during the twentieth century. *Theoretical and Applied Climatology*, *98*, 119–135.

Korecha, D., & Barnston, A. G. (2007). Predictability of june–september rainfall in Ethiopia. *Monthly Weather Review*, *135*(2), 628–650.

Mann, H. B. (1945). Nonparametric tests against trend. *Econometrica: Journal of the Econometric Society*, 245–259.

Mesfin, D., Simane, B., Belay, A., Recha, J. W., & Schmiedel, U. (2020). Assessing the adaptive capacity of households to climate change in the Central Rift Valley of Ethiopia. *Climate*, *8*(10), 106.

Mohammed, Y., Yimer, F., Tadesse, M., & Tesfaye, K. (2019). Variability and trends of

rainfall extreme events in north east highlands of Ethiopia. *International Journal of Hydrology*, *2*(5), 594–605. https://doi.org/10.15406/ijh.2018.02.00131

Moloro, T. L. (2018). Spatio-temporal analysis of rainfall variability and meteorological drought: a case study in Bilate River Basin, Southern Rift Valley, Ethiopia. *International Journal of Environmental Sciences & Natural Resources*, *14*(4), 76–89.

Montgomery, S. B., Goode, D. L., Kvikstad, E., Albers, C. A., Zhang, Z. D., Mu, X. J., Ananda, G., Howie, B., Karczewski, K. J., & Smith, K. S. (2013). The origin, evolution, and functional impact of short insertion–deletion variants identified in 179 human genomes. *Genome Research*, *23*(5), 749–761.

Mulugeta, S., Fedler, C., & Ayana, M. (2019). Analysis of long-term trends of annual and seasonal rainfall in the Awash River Basin, Ethiopia. *Water*, *11*(7), 1498.

NOAA. (2023). *2022 NOAA Science Report*. 81. https://sciencecouncil.noaa.gov/wp-content/uploads/2023/03/FINAL_2022-NOAA-Science-Report.pdf

Roundy, P. E. (2015). On the interpretation of EOF analysis of ENSO, atmospheric Kelvin waves, and the MJO. *Journal of Climate*, *28*(3), 1148–1165.

Saji, N. H., & Vinayachandran, P. N. (1999). *A dipole mode in the tropical Indian Ocean*. *401*(September), 360–363.

Sen, P. K. (1968). Estimates of the regression coefficient based on Kendall's tau. *Journal of the American Statistical Association*, *63*(324), 1379–1389.

Senbeta, A. F., Worku, W., & Gayler, S. (2024a). Spatiotemporal climate variability and food security implications in the Central Ethiopia Region. *Scientific African*, *26*(September), e02390. https://doi.org/10.1016/j.sciaf.2024.e02390

Senbeta, A. F., Worku, W., & Gayler, S. (2024b). Spatiotemporal climate variability and food security implications in the Central Ethiopia Region. *Scientific African*, *26*(September). https://doi.org/10.1016/j.sciaf.2024.e02390

Senbeta, A. F., Worku, W., Gayler, S., & Naimi, B. (2024). Unveiling Wheat's Future Amidst Climate Change in the Central Ethiopia Region. *Agriculture*, *14*(8), 1408.

Stuecker, M. F., Timmermann, A., Jin, F., Chikamoto, Y., Zhang, W., Wittenberg, A. T., Widiasih, E., & Zhao, S. (2017). Revisiting ENSO/Indian Ocean dipole phase relationships. *Geophysical Research Letters*, *44*(5), 2481–2492.

Tate, E. L., Sene, K. J., & Sutcliffe, J. V. (2001). A water balance study of the upper White Nile basin flows in the late nineteenth century. *Hydrological Sciences Journal*, *46*(2), 301–318.

Ware, M. B., Mori, P., Warrach-Sagi, K., Jury, M., Schwitalla, T., Beyene, K. H., & Wulfmeyer, V. (2022). Climate regionalization using objective multivariate clustering methods and characterization of climatic regions in Ethiopia. *Meteorol. Z*, *31*, 431–453.

Weldegerima, T. M., Zeleke, T. T., Birhanu, B. S., Zaitchik, B. F., & Fetene, Z. A. (2018). Analysis of rainfall trends and its relationship with SST signals in the Lake Tana Basin, Ethiopia. *Advances in Meteorology*, *2018*(1), 5869010.

Wilks, D. S. (2011). Forecast verification. In *International geophysics* (Vol. 100, pp. 301–394). Elsevier.

Worku, M. A., Feyisa, G. L., Beketie, K. T., & Garbolino, E. (2022). Rainfall variability and trends in the Borana zone of southern Ethiopia. *Journal of Water and Climate Change*, *13*(8), 3132–3151. https://doi.org/10.2166/wcc.2022.173

Yi, W., & Zhong-Wei, Y. (2009). Trends in seasonal precipitation over China during 1961-2007. *Atmospheric and Oceanic Science Letters*, *2*(3), 165–171.

Yirga, S. A. (2021). Spatio-temporal analysis of drought variability in central Ethiopia. *Journal of Water and Climate Change*, *12*(5), 1778–1787. https://doi.org/10.2166/wcc.2020.226

Yosef, G., Alpert, P., Price, C., Rotenberg, E., & Yakir, D. (2017). Using EOF analysis over a large area for assessing the climate impact of small-scale afforestation in a semiarid region. *Journal of Applied Meteorology and Climatology*, *56*(9), 2545–2559.

Zeleke, A., Tesfaye, K., Tadesse, T., Alem, T., Ademe, D., & Adgo, E. (2023). Spatiotemporal analysis of rainfall and temperature variability and trends for climate resilient maize farming system in major agroecology zones of northwest Ethiopia. *International Journal of Agricultural Sustainability*, *21*(1), 2255450.

Zeleke, T., Giorgi, F., Mengistu Tsidu, G., & Diro, G. T. (2013). Spatial and temporal variability of summer rainfall over Ethiopia from observations and a regional climate model experiment. *Theoretical and Applied Climatology*, *111*, 665–681.